NAWCWD TP 8502

Radar Scattering Center Localization by Subspace Fitting

by

Brett Borden
Research Department

AUGUST 2001

NAVAL AIR WARFARE CENTER WEAPONS DIVISION
CHINA LAKE, CA 93555-6100

Approved for public release; distribution is unlimited.

Naval Air Warfare Center Weapons Division

FOREWORD

The research described in this report was performed during the 2000-2001 fiscal years as part of an effort supported by the Office of Naval Research funding document numbers N0001401WR20168 and N0001400WR20063 to improve radar classification and identification capabilities for noncooperative airborne targets. This continues to be a primary goal of radar research programs and considerable effort has been expended within the last few decades. The accuracy of any radar imaging method depends in a sensitive way upon available radar resolution and signal-to-noise ratio.

The current work describes an algorithm for determining the position and strength of radar target scattering centers from low resolution and noise corrupted data. The technique is remarkably stable against very poor signal-to-noise ratios and offers good super resolution capabilities.

This report was reviewed for technical accuracy by Carey Schwartz.

Approved by
C. F. MARKARIAN, *Head*
Research Department
31 August 2001

Under authority of
C. H. JOHNSTON, JR
RADM (sel), U.S. Navy
Commander

Released for publication by
K. L. HIGGINS
Director for Research and Engineering

NAWCWPNS Technical Publication 8502

Published by . . . . . Technical Information Division
Collation . . . . . Cover, 7 leaves
First printing . . . . . 25 copies

REPORT DOCUMENTATION PAGE

Form Approved
OMB No. 0704-0188

1. AGENCY USE ONLY *(Leave blank)*	2. REPORT DATE	3. REPORT TYPE AND DATES COVERED
	AUGUST 2001	Interim Oct 99-Apr 01

4. TITLE AND SUBTITLE
Radar Scattering Center Localization by Subspace Fitting (U)

5. FUNDING NUMBERS
N0001401WR20168
N0001400WR20063

6. AUTHOR(S)
Brett Borden

7. PERFORMING ORGANIZATION NAME(S) AND ADDRESS(ES)
Naval Air Warfare Center Weapons Division
China Lake, CA 93555-6100

8. PERFORMING ORGANIZATION REPORT NUMBER
NAWCWPNS TP 8502

9. SPONSORING/MONITORING AGENCY NAME(S) AND ADDRESS(ES)
Office of Naval Research
800 N. Quincy
Arlington, VA

10. SPONSORING/MONITORING AGENCY REPORT NUMBER

11. SUPPLEMENTARY NOTES

12A. DISTRIBUTION/AVAILABILITY STATEMENT
A Statement; public release; distribution unlimited.

12B. DISTRIBUTION CODE

13. ABSTRACT *(Maximum 200 words)*

(U) The application of radar data to the problem of noncooperative target recognition (NCTR) usually begins by estimating the position and strength of the significant scattering centers from the bright spot locations of a radar image (e.g., high range resolution (HRR) or inverse synthetic aperture radar (ISAR)). In practical situations, these images are usually contaminated by noise and can be of very low quality resolution—factors that confound the scattering center localization process and can preclude NCTR by radar means. We describe a simple method, based on subspace fitting techniques, that can be applied to the position and strength estimation problem in this environment. The scheme is robust against noise corruption and allows for super-resolved estimates of all (or some) of the scatterers. Examples based on synthetic data are presented.

14. SUBJECT TERMS
Radar imaging, ISAR, HRR
Superresolution, SAR
Subspace fitting, NCTR

15. NUMBER OF PAGES
14

16. PRICE CODE

17. SECURITY CLASSIFICATION OF REPORT	18. SECURITY CLASSIFICATION OF THIS PAGE	19. SECURITY CLASSIFICATION OF ABSTRACT	20. LIMITATION OF ABSTRACT
UNCLASSIFIED	UNCLASSIFIED	UNCLASSIFIED	UL

INTRODUCTION

In the past few decades, considerable attention has been paid to the problem of obtaining accurate and high resolution radar images of complex targets (cf, References 1 through 3, and references cited therein). When the ultimate goal is radar-based target recognition, however, even high quality radar images generally contain enough erroneous and surplus information to prevent the use of practical template-based matching algorithms (References 4 and 5). In this situation, the conventional heuristic remedy truncates these images into a small set of basic image "features," including points, plates, dihedrals, single and doubly curved surfaces, edges, and corners (References 2 and 4 through 7). In noisy and data-limited environments, practical considerations preclude distinguishing these scattering mechanisms (References 1, 6, and 8), and the most common set of image features is formed from estimates of the position and strength of target scattering centers (assumed to behave as noninteracting point subtargets).

But, when the radar image is of low resolution and contaminated with noise-induced artifacts, it can also be very difficult to accurately estimate either the position or strength of the scattering centers. Of course, this estimation error is directly related to the efficacy of template-based target identification methods and can preclude such systems from application in many real-world environments for which radar is the only otherwise viable sensor.

Below, we will briefly review the problem of radar image formation. This review will serve to define the problem and establish notational conventions. Using this framework, we will then describe a method for accurately estimating the position and strength of target scattering centers directly from measured radar data. Examples of dependence on noise, resolution, and scatterer number assumptions are also presented.

RADAR DATA AND THE LINEAR SCATTERING MODEL

For notational simplicity, we consider a monostatic scattering configuration in which the radar transmitter is co-located with the receiver. Denote by $s_{\mathrm{r}}(t)$ the signal received by the radar at time t and let $s_{\mathrm{scatt}}(t)$ be the response signal of the target to an incident interrogating signal $s_{\mathrm{inc}}(t)$. The original radar signal processing problem is that of optimal detection in (additive) noise so that the received data are of the form: $s_{\mathrm{r}}(t) = s_{\mathrm{scatt}}(t) + n(t)$, where $n(t)$ is a random noise process.

In conventional radar systems, "optimal detection" has been accomplished through maximum likelihood methods that compare $s_{\mathrm{r}}(t)$ to an idealized family of signals predicted using a model $\mathcal{M}$. We assume that $\mathcal{M}$ is unique and let $p_{s_{\mathrm{ideal}}|s_{\mathrm{r}}}(\mathcal{M})$ denote the *a posteriori* conditional probability density of $s_{\mathrm{ideal}}(t)$ given $s_{\mathrm{r}}(t)$ (the *a posteriori* density is determined by the statistics of $n(t)$ and *a priori* target estimates (Reference 9)). Then the maximum likelihood model satisfies

$$\mathcal{M}_{\mathrm{ML}} = \arg \max_{u \in \text{model space}} p_{s_{\mathrm{ideal}}|s_{\mathrm{r}}}(u) \tag{1}$$

It is usual to parameterize the model space to facilitate the search for $\mathcal{M}_{\mathrm{ML}}$. In active radar, the natural parameterization is based on the scattering interaction between the interrogating field

and the target's reflectivity behavior. The simplest version of this interaction is the linear radar (weak-scatterer) scattering model that relates $s_{\text{scatt}}(t)$ to $s_{\text{inc}}(t)$ by

$$s_{\text{scatt}}(t) = \int_{\mathbb{R}^2} \varrho_s(t', \nu')\, s_{\text{inc}}(t - t')\, \mathrm{e}^{\mathrm{i}\nu'(t-t')} \mathrm{d}t' \mathrm{d}\nu' \tag{2}$$

where $\varrho_s(t, \nu)$ is the target reflectivity density defined in such a way that $\varrho_s(t, \nu)\mathrm{d}t\mathrm{d}\nu$ is proportional to the field reflected from the target at range between $ct/2$ and $c(t+\mathrm{d}t)/2$ with Doppler shift between ν and $\nu + \mathrm{d}\nu$. In general, the reflectivity density actually depends upon the incident field. But when these nonlinear effects can be neglected, the ML model also yields the maximum detection signal-to-noise ratio and, in the Gaussian white noise and no prior target information case, correlation receivers (References 9 through 11) attempt to find the t and ν that maximize the real part of

$$\eta(t, \nu) = \int_{\mathbb{R}} s_{\text{r}}(t')\, s^*_{\text{inc}}(t' - t) \mathrm{e}^{-\mathrm{i}\nu(t'-t)} \mathrm{d}t' \tag{3}$$

To understand just what it is that the correlation receiver "sees," substitute the model of Equation 2 into Equation 3 to yield

$$\eta(t, \nu) = \int_{\mathbb{R}^2} \varrho_s(t', \nu')\, \chi(t - t', \nu - \nu')\, \mathrm{e}^{\mathrm{i}(\nu+\nu')(t-t')/2} \mathrm{d}t' \mathrm{d}\nu' \tag{4}$$

where

$$\chi(t, \nu) \equiv \int_{\mathbb{R}} s^*_{\text{inc}}(t' - \tfrac{1}{2}t)\, s_{\text{inc}}(t' + \tfrac{1}{2}t)\, \mathrm{e}^{-\mathrm{i}\nu t'} \mathrm{d}t' \tag{5}$$

and we have suppressed an additive noise function (for the present).

Equation 4 is an imaging equation in which $\varrho_s(t, \nu)$ is the object function and the remaining factors in the integrand represent an imaging kernel (a point-spread function). Consequently, $\eta(t, \nu)$ is an estimate of $\varrho_s(t, \nu)$ and we can write $\hat{\varrho}_s(t, \nu) = \eta(t, \nu)$. The ideal imaging kernel would be given by $\chi(t, \nu) = \delta(t)\delta(\nu)$, but there is a well-known limit to the "narrowness" of the peak of $|\chi(t, \nu)|$ that can be (simultaneously) attained in the t and ν directions. This *ambiguity relation* means that an interrogating signal $s_{\text{inc}}(t)$ that leads to good resolution in the t-direction will generally have poor resolution in the ν-direction, and vice versa.

A method for getting around this fundamental limitation selects a *family* of signals $s_\theta(t)$, parameterized by θ, which lead to $\chi_\theta(t, \nu)$ that are independently localized along different directions with respect to target orientation. In Inverse Synthetic Aperture Radar (ISAR) imaging, for example, the parameter θ is target angular aspect, which varies in time if the target is rotating. The radar is (usually) configured to transmit a series of pulses $s(t - j\Delta t)$, $j = 1, \ldots, \Theta$, with good range resolution but poor cross-range (Doppler) resolution. Assume, for simplicity, a constant target rotation rate $\dot{\theta} = \Omega$. Assume also that the scattering components that make up the target are *persistent* (i.e.,

independent of θ over the aperture $\Delta\theta = (\Theta - 1)\Delta t\,\Omega$). Then the jth pulse will interrogate the rotated object function $\varrho_\theta(t,\nu) = \rho(t\cos\theta_j + \alpha^{-1}\nu\sin\theta_j, -\alpha t\sin\theta_j + \nu\cos\theta_j)$ where $\theta_j = j\Delta t\,\Omega$ and $\alpha \propto \Omega$ is a scale factor relating target dimensions in t to those in ν. Equation 4 becomes

$$\eta_{\theta_j}(t,\nu) = \int_{\mathbb{R}^2} \rho(t'\cos\theta_j + \alpha^{-1}\nu'\sin\theta_j, -\alpha t'\sin\theta_j + \nu'\cos\theta_j) \times \mathrm{e}^{\mathrm{i}(\nu+\nu')(t-t')/2}\,\chi(t-t', \nu-\nu')\,\mathrm{d}t'\mathrm{d}\nu' \tag{6}$$

Substituting the idealization $\chi(t,\nu) = \delta(t)$ yields

$$\eta_{\theta_j}(t,\nu) = \int_{L(t;\theta_j)} \rho(t',\nu')\,\mathrm{d}l \tag{7}$$

where $\mathrm{d}l$ is the differential arc length along the line $L(t;\theta_j) = \{(t',\nu') \,|\, t'\cos\theta_j + \nu'\sin\theta_j = t\}$. Equation 7 is the idealized *range profile* of the target at aspect θ and it is easy to see the relationship between ISAR imagery and tomographic reconstruction from this expression (note that Equation 7 is actually independent of ν).

Realizable measurement systems will obtain finite and band-limited data, of course, and will be unable to generate true δ-functions in the time-domain. This situation has an idealization that uses incident radar signals of the (frequency-domain) form

$$S(\omega) = \mathcal{F}\{s\}(\omega) = \sqrt{\frac{2\pi}{\Delta\omega}}\,\mathrm{rect}\left(\frac{\omega-\omega_0}{\Delta\omega}\right) \qquad \omega \in (\omega_1, \omega_2) \tag{8}$$

where $\mathcal{F}$ denotes the Fourier transform operation, $\Delta\omega = \omega_2 - \omega_1$, $\omega_0 = \frac{1}{2}(\omega_1 + \omega_2)$, and $\mathrm{rect}(x) = 1$ if $x \in (-\frac{1}{2}, \frac{1}{2})$ and 0 otherwise. The $\chi(t,\nu)$ associated with this signal is

$$\chi(t,\nu) = \frac{\Delta\omega - |\nu|}{\Delta\omega}\,\mathrm{e}^{\mathrm{i}(\omega_0+\nu/2)t}\,\mathrm{sinc}\left[\tfrac{1}{2}(\Delta\omega - |\nu|)t\right], \qquad |\nu| \leqslant \Delta\omega \tag{9}$$

where $\mathrm{sinc}(x) = \sin x/x$.

By increasing the bandwidth $\Delta\omega$, the kernel $\chi(t,\nu)$ given by Equation 9 can be made to more closely approximate $\delta(t)$. The cross-range resolution, which is determined by $\Delta\theta$, cannot generally be specified as part of the radar system design and ISAR imaging systems must often spend impractically long time intervals waiting for the target to rotate. More typically, ISAR imaging practitioners simply resign themselves to low cross-range image resolutions.

TARGET MODEL BASED SIMPLIFICATION

Considerable further simplification occurs when the object function can also be replaced by a lower dimension parameterization. Heuristic arguments (References 1 through 8) have been made for replacing the weak scatterer reflectivity density by the scattering behavior associated with a collection of non-interacting characteristic shapes. The simplest, and most common, choice for these shapes is point scatterers (or, more correctly, point scatterer behavior over the range of frequencies and aspects of the observation). In limited and noisy data situations, the point scatterer model is a practical expedient—and may be a necessity (Reference 6 and 8). Assuming this model approximation is accurate, we can write

$$\varrho(t,\nu) = \sum_{n=1}^{N} a_n \delta(\nu - x_n)\delta(t - y_n) \tag{10}$$

where $a_n \in \mathbb{C}$ is the local scatterer strength and the sum is over all N scattering centers.

Substituting the model 10 into Equation 6 (with the rotated object function) yields

$$\eta_\theta(t,\nu) = \sum_{n=1}^{N} a_n \, \chi(t - u_n, \nu - v_n)\, \mathrm{e}^{\mathrm{i}(\nu+v_n)(t-u_n)/2} \qquad \text{for} \quad \theta = \theta_1, \theta_2 \ldots, \theta_\Theta \tag{11}$$

where $u_n(\theta) \equiv -x_n \sin\theta + y_n \cos\theta$, and $v_n(\theta) \equiv x_n \cos\theta + y_n \sin\theta$. To simplify our notation, we consider $\mathbf{s}_\mathrm{r}$, $\mathbf{s}_\mathrm{scatt}$, and $\mathbf{n}$ to be members of $L^2(\mathcal{T})$ where $\mathcal{T} \subset \mathbb{R}$. Let $[\mathbf{x}]_n = x_n$, $[\mathbf{y}]_n = y_n$, and define the matrix

$$[\boldsymbol{\chi}_\theta(\mathbf{x},\mathbf{y})]_{t,n} = \chi(t - u_n, \nu - v_n)\, \mathrm{e}^{\mathrm{i}(\nu+v_n)(t-u_n)/2} \tag{12}$$

If we construct the concatenated matrices

$$\boldsymbol{\chi}(\mathbf{x},\mathbf{y}) = \begin{bmatrix} \boldsymbol{\chi}_{\theta_1}(\mathbf{x},\mathbf{y}) \\ \boldsymbol{\chi}_{\theta_2}(\mathbf{x},\mathbf{y}) \\ \vdots \\ \boldsymbol{\chi}_{\theta_\Theta}(\mathbf{x},\mathbf{y}) \end{bmatrix}, \qquad \text{and} \qquad \boldsymbol{\eta} = \begin{bmatrix} \boldsymbol{\eta}_{\theta_1} \\ \boldsymbol{\eta}_{\theta_2} \\ \vdots \\ \boldsymbol{\eta}_{\theta_\Theta} \end{bmatrix} \tag{13}$$

where $[\boldsymbol{\eta}_\theta]_t = \eta_\theta(t,\nu)$, then Equation 11 can be written as

$$\boldsymbol{\eta} = \boldsymbol{\chi}(\mathbf{x},\mathbf{y})\,\mathbf{a} + \mathbf{n} \tag{14}$$

where $[\mathbf{a}]_n = a_n$ and we have re-introduced the noise function term for completeness.

An effective method for estimating the model parameters $\{a_n, x_n, y_n\}_{n=1,\ldots,N}$ is to separate the linear components a_n from the x_n, y_n (Reference 12). *Formally,* we can write the least squares solution to Equation 14 as

$$\hat{\mathbf{a}} = \left(\boldsymbol{\chi}^\dagger(\mathbf{x},\mathbf{y})\boldsymbol{\chi}(\mathbf{x},\mathbf{y})\right)^{-1}\boldsymbol{\chi}^\dagger(\mathbf{x},\mathbf{y})\,\boldsymbol{\eta} \equiv \boldsymbol{\chi}^-(\mathbf{x},\mathbf{y})\,\boldsymbol{\eta} \tag{15}$$

where $\boldsymbol{\chi}^\dagger = (\boldsymbol{\chi}^*)^\top$ and $\boldsymbol{\chi}^-(\mathbf{x},\mathbf{y}) = \left(\boldsymbol{\chi}^\dagger(\mathbf{x},\mathbf{y})\boldsymbol{\chi}(\mathbf{x},\mathbf{y})\right)^{-1}\boldsymbol{\chi}^\dagger(\mathbf{x},\mathbf{y})$ is the pseudoinverse of $\boldsymbol{\chi}(\mathbf{x},\mathbf{y})$. Consequently, the $\mathbf{a}$ can be eliminated and an estimate of $\mathbf{x}$ and $\mathbf{y}$ can be determined by minimizing

$$\|\boldsymbol{\eta} - \boldsymbol{\chi}(\mathbf{x},\mathbf{y})\,\mathbf{a}\|^2 = \|\boldsymbol{\eta} - \boldsymbol{\chi}(\mathbf{x},\mathbf{y})\,\boldsymbol{\chi}^-(\mathbf{x},\mathbf{y})\,\boldsymbol{\eta}\|^2 = \|\left(\mathbf{I} - \mathbf{P}(\mathbf{x},\mathbf{y})\right)\boldsymbol{\eta}\|^2 \tag{16}$$

where

$$\mathbf{P}(\mathbf{x},\mathbf{y}) = \boldsymbol{\chi}(\mathbf{x},\mathbf{y})\,\boldsymbol{\chi}^-(\mathbf{x},\mathbf{y}) \tag{17}$$

is the orthogonal projection on the linear subspace spanned by the columns of the matrix $\boldsymbol{\chi}(\mathbf{x},\mathbf{y})$.

Once the scattering center position estimates $\hat{\mathbf{x}}, \hat{\mathbf{y}}$ are obtained, the scatterer strength can then be estimated using Equation 15.

NUMERICAL ALGORITHM

When the image is to be used for identification purposes, the dimension N of model parameters will usually be selected to be small (in comparison with the dimension M of the data collected). The problem of finding the minimum of Equation 16 can be efficiently handled in terms of the QR decomposition (Reference 13).

By construction, the rank of $\boldsymbol{\chi} \in \mathbb{C}^{M\times N}$ is N. In this case, we can write

$$\boldsymbol{\chi} = \mathbf{Q}\begin{bmatrix}\mathbf{R}\\ \hline \mathbf{0}\end{bmatrix} \tag{18}$$

where $\mathbf{Q} \in \mathbb{C}^{M\times M}$ is unitary, $\mathbf{R} \in \mathbb{C}^{N\times N}$ is a nonsingular upper triangular matrix, and the lower partition is the $(M-N)\times N$ zero matrix.

In terms of this decomposition, the pseudoinverse of $\boldsymbol{\chi}$ can be expressed as

$$\boldsymbol{\chi}^- = \left[\mathbf{R}^{-1}\,|\,\mathbf{0}\right]\mathbf{Q}^\dagger \tag{19}$$

Substituting the decomposition of Equation 18 into 17, it is easy to show that

$$\mathbf{P} = \mathbf{Q}\begin{bmatrix}\mathbf{I}_N & \mathbf{0}\\ \mathbf{0} & \mathbf{0}\end{bmatrix}\mathbf{Q}^\dagger \qquad \text{and} \qquad \mathbf{I}-\mathbf{P} = \mathbf{Q}\begin{bmatrix}\mathbf{0} & \mathbf{0}\\ \mathbf{0} & \mathbf{I}_{M-N}\end{bmatrix}\mathbf{Q}^\dagger \tag{20}$$

where $\mathbf{I}_N$ is the $N \times N$ identity matrix. Because $\mathbf{Q}$ is unitary, then $\|\mathbf{Qw}\| = \|\mathbf{w}\|$ for all vectors $\mathbf{w}$ and, consequently, from Equations 16 and 20 we have

$$\hat{\mathbf{x}}, \hat{\mathbf{y}} = \arg\min_{\mathbf{x},\mathbf{y}} \left\| \begin{bmatrix}\mathbf{0} & \mathbf{0}\\ \mathbf{0} & \mathbf{I}_{M-N}\end{bmatrix}\mathbf{Q}^\dagger\boldsymbol{\eta}\right\|^2 \tag{21}$$

The gradient of $r(\mathbf{x},\mathbf{y}) = \|\mathbf{r}(\mathbf{x},\mathbf{y})\|^2 \equiv \|(\mathbf{I}-\mathbf{P}(\mathbf{x},\mathbf{y}))\boldsymbol{\eta}\|^2$ is given by (Reference 12)

$$\boldsymbol{\nabla} r(\mathbf{x},\mathbf{y}) = -2\mathrm{Re}\left\{\boldsymbol{\eta}^\dagger(\mathbf{I}-\mathbf{P})\mathbf{D}\boldsymbol{\chi}(\mathbf{x},\mathbf{y})\,\boldsymbol{\chi}^-(\mathbf{x},\mathbf{y})\boldsymbol{\eta}\right\} \tag{22}$$

where

$$[\mathbf{D}\boldsymbol{\chi}]_{i,k,j} \equiv [\boldsymbol{\nabla}\chi_{i,j}]_k \tag{23}$$

and $\chi_{i,j} = [\boldsymbol{\chi}]_{i,j}$. In terms of Equations 18 through 20, we can write

$$\boldsymbol{\nabla} r(\mathbf{x},\mathbf{y}) = -2\mathrm{Re}\left\{\left(\mathbf{Q}\begin{bmatrix}\mathbf{0} & \mathbf{0}\\ \mathbf{0} & \mathbf{I}_{M-N}\end{bmatrix}\mathbf{Q}^\dagger\boldsymbol{\eta}\right)^\dagger \mathbf{D}\boldsymbol{\chi}(\mathbf{x},\mathbf{y})\,\left[\mathbf{R}^{-1}\,|\,\mathbf{0}\right]\mathbf{Q}^\dagger\boldsymbol{\eta}\right\} \tag{24}$$

If we denote the number of time samples per aspect by T (so that $M = T \times \Theta$) then from Equations 12 and 13 we have

$$\begin{aligned}\boldsymbol{\nabla}\chi_{i,j} = &\left(-\frac{\partial\chi(t',\nu')}{\partial t'} - \tfrac{1}{2}\mathrm{i}(\nu'+2v_j)\,\chi(t',\nu')\right)\\ &\quad\times \mathrm{e}^{\mathrm{i}(\nu'+2v_j)t'/2}\,(-\hat{\mathbf{x}}\sin\theta + \hat{\mathbf{y}}\cos\theta)\\ &+\left(-\frac{\partial\chi(t',\nu')}{\partial\nu'} + \tfrac{1}{2}\mathrm{i}t'\,\chi(t',\nu')\right)\\ &\quad\times \mathrm{e}^{\mathrm{i}(\nu'+2v_j)t'/2}\,(\hat{\mathbf{x}}\cos\theta + \hat{\mathbf{y}}\sin\theta)\Big|_{\substack{t'=t_{1+(i-1)\bmod T}-u_j(\theta_{1+\mathrm{int}(i/T)})\\ \nu'=\nu-v_j(\theta_{1+\mathrm{int}(i/T)})\\ \theta=\theta_{1+\mathrm{int}(i/T)}}}\end{aligned} \tag{25}$$

where int(w) denotes the integer part of w and $\hat{\mathbf{x}}$ and $\hat{\mathbf{y}}$ are the unit direction vectors.

The gradient of r (Equation 22) can be used in standard iterative schemes for finding $\arg\min_{\mathbf{x},\mathbf{y}} r$. Quasi-Newton methods, for example, set the $j+1$ estimate $\mathbf{z}^{(j+1)}$ in terms of the previous estimate $\mathbf{z}^{(j)}$ by (cf, Reference 14)

$$\mathbf{z}^{(j+1)} = \mathbf{z}^{(j)} - \alpha^{(j)} \mathbf{H}^{-1\,(j)} \nabla r^{(j)} \tag{26}$$

where $\mathbf{H}^{-1\,(j)} = \mathbf{H}^{-1}(\mathbf{z}^{(j)})$ is the inverse of the Hessian, $\nabla r^{(j)} = \nabla r(\mathbf{z}^{(j)})$, and $\alpha^{(j)} > 0$ defines a step size. Usually, the Hessian is estimated numerically and $\alpha^{(j)}$ is chosen so that r achieves a local minimum along the direction $-\mathbf{H}^{-1\,(j)} \nabla r^{(j)}$ from $\mathbf{z}^{(j)}$.

An efficient implementation of Equations 16, 24 and 25, using Householder transformations, is presented in the Appendix. Most of the elements of the tensor $\mathbf{D}\boldsymbol{\chi}$ will have zero value and the routine accounts for this by tracking only the nonzero terms: it has memory requirements of approximately $(3N+1) \times M$ complex values plus an additional $2M$ complex workspace requirement. The algorithm-specific computational demands are dominated by the QR decomposition, which requires $O(N^2(M - N/3))$ floating point operations. Of course, the calculation of $\mathbf{D}\boldsymbol{\chi}$ generally depends on the form of χ and the implementation (and approximations) that best match its evaluation. (In our case, the straightforward calculation of $\nabla\chi$ that we employed (cf the Appendix) accounts for more than 98% of the CPU usage—implementations more appropriate to real time environments are straightforward (e.g., lookup tables).)

SAMPLE RESULTS

We generated synthetic data η_{SNR} from Equation 14 using a point target model characterized by $\mathbf{x}$, $\mathbf{y}$, and $\mathbf{a}$. The additive noise term was fabricated using a Gaussian noise generator and had energy determined by a signal-to-noise ratio (SNR) defined so that

$$\mathrm{SNR} = \frac{(\boldsymbol{\chi}(\mathbf{x},\mathbf{y})\,\mathbf{a})^{\dagger}\,\boldsymbol{\chi}(\mathbf{x},\mathbf{y})\,\mathbf{a}}{\mathbf{n}^{\dagger}\mathbf{n}} \tag{27}$$

All of our examples were formed from data constructed with the *scaled* parameter values: $\nu = 0$, $t \in (-.5, .5)$, $\theta \in (-4°, 4°)$, $\Delta\omega = 4\pi$, and $\omega_0 = 10\Delta\omega$ (e.g., roughly consistent with a 3-meter sized target interrogated with a signal bandwidth equal to 10% of a center frequency equal to 2 GHz). The radar ambiguity function was modeled by Equation 9.

A variety of nonlinear optimization approaches were tried and all yielded similar results. The figures below were created from the solutions found using the iteration scheme of Equation 26 with a Broyden-Fletcher-Goldfarb-Shanno (BFGS) Hessian updating scheme and an Armijo's rule line search for determining $\alpha^{(j)}$ (Reference 14).

Figure 1 displays the estimates for four different values of SNR (SNR $= 10, 1, 0.1, 0.01$). The baseplane (x–y plane) of each figure contains the (gray-scale encoded) intensity values of the traditional (ISAR) image, $I_{\mathrm{ISAR}}(x,y)$, formed by applying the standard convolution-backprojection algorithm to the η_{SNR}. The peak values of I_{ISAR} are plotted against the back walls of the figure: $P_x(y) = \max_x |I_{\mathrm{ISAR}}(x,y)|$ is displayed in the $x = 0.5$ plane; and $P_y(x) = \max_y |I_{\mathrm{ISAR}}(x,y)|$ is

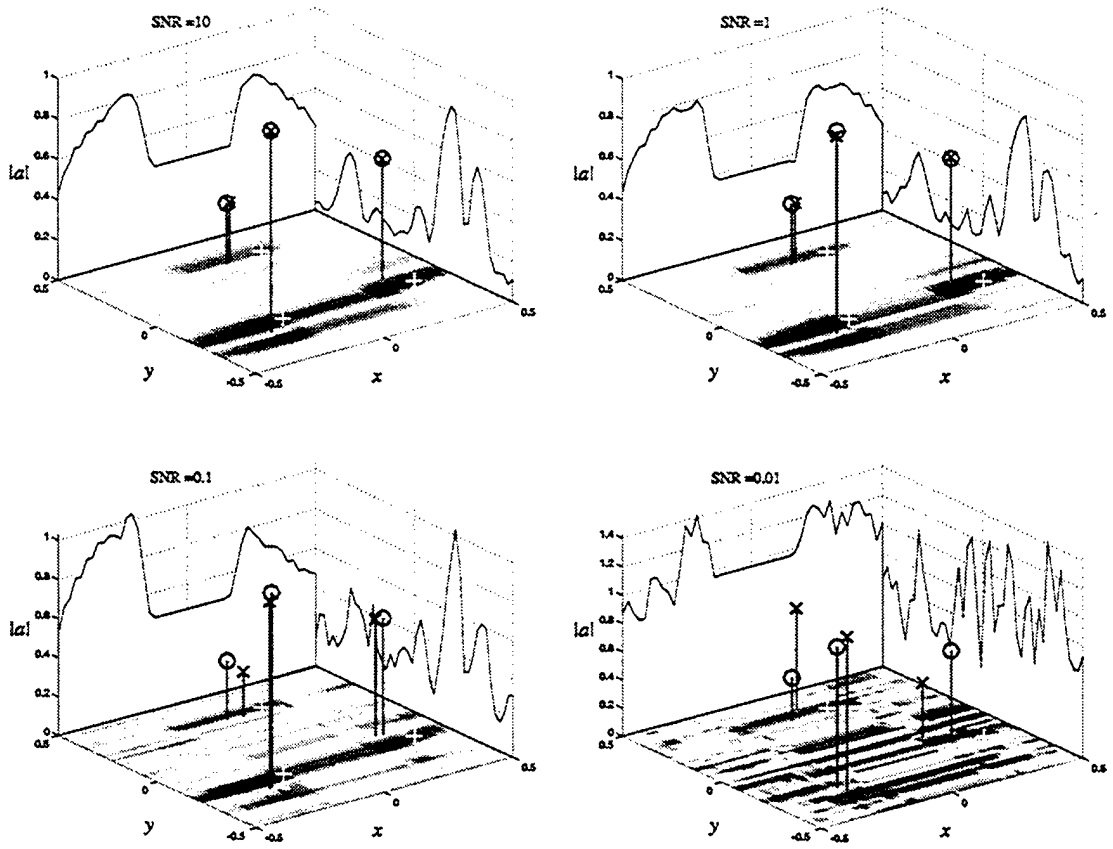

FIGURE 1. A Simple Example of Scattering Center Estimation in Noisy, Low Resolution Situations Based on Simulated Radar Data. The traditional ISAR image is displayed in the baseplane, while the projected ISAR image intensity is displayed in the backplanes. The actual scattering centers are marked with the symbol "○," while the estimates values are plotted using "×." Iteration starting points are marked with "+."

displayed in the $y = 0.5$ plane. The true values of $\{x_n, y_n, |a_n|\}$ are plotted using the symbol "○," while the estimated values are plotted using "×." The seed values for $\mathbf{x}$ and $\mathbf{y}$ are displayed using "+" in the base plane.

The results shown in Figure 1 are typical of all the tests we performed and reflect a graceful localization failure with increasing noise contamination. Our experience is that noise contamination generally does not significantly alter the character of the hypersurface r but, instead, only moves the local minimum (of course, it also introduces a constant offset). Figure 2 illustrates this behavior and is a plot of a one-dimensional cut through the surface r for different values of SNR. (The strength and location of the scattering centers in Figure 2 are the same as those used in Figure 1.) Because of this graceful localization failure with increasing noise, the practical limitation of the method results from the effects of noise on the *traditional* ISAR image, because a low quality image can prevent an estimate of N and the seed values for $\mathbf{x}$ and $\mathbf{y}$. (In general, we found the algorithm to be robust against seed value choice, although solution speed was somewhat altered.)

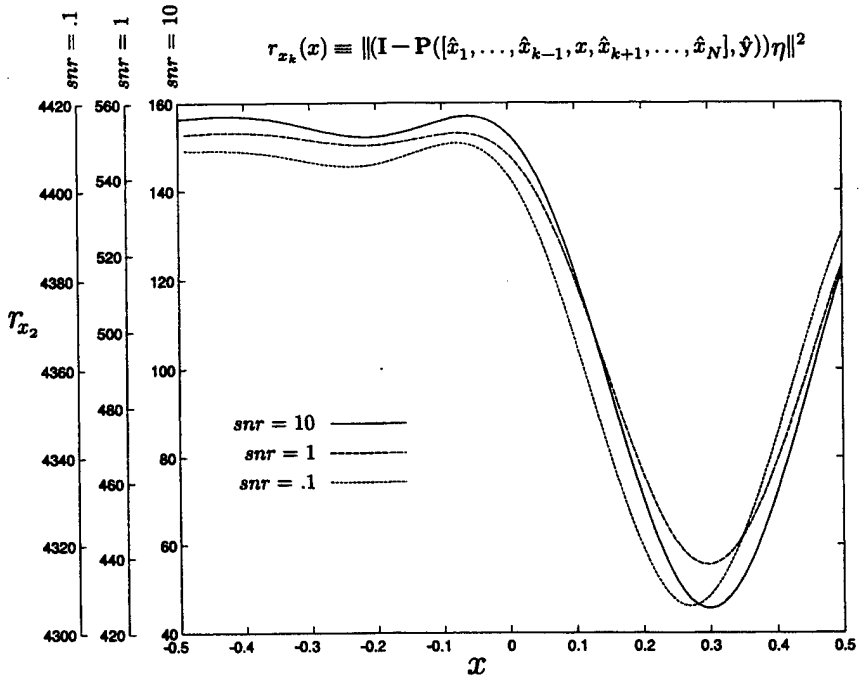

FIGURE 2. The Cost Function for Various SNRs. Plotted are 1-D cuts through r.

When the SNR is favorable, however, the method can be an effective localizer and will usually surpass the standard resolution limitations of an ISAR image. Figure 3(a) shows the "super-resolution" capabilities of the algorithm. The x and y resolution cells associated with these data are $\Delta x \approx 2\pi c(\omega_0 \Delta\theta)^{-1} \approx 0.36$ and $\Delta y \approx \pi c(2\Delta\omega)^{-1} \approx 0.12$, respectively. The actual scatterers were separated by $x_1 - x_2 = 0.05 \approx \Delta x/7$ and $y_1 - y_2 = 0.03 \approx \Delta y/4$. Of course, super-resolution requires that the user have some prior reason to suspect that there is more than one scatterer in a particular target region—this information surely cannot be divined from the raw ISAR image, and the model order N must be set in advance (along with seed guesses). Figure 3(b) shows the results of estimating N to be larger than its correct value (in this case, $N_{\text{est}} = 2$, $N_{\text{actual}} = 1$). Observe that the algorithm correctly fits one of the scatterers to the data and assigns a strength of $|a_2| = 0$ to the other. (It is possible for the method to converge to different results, but the behavior of Figure 3(b) was the most commonly observed.)

CONCLUSION

Traditionally, even the simple problem of fitting a point scatterer model to ISAR data has frequently proven impracticable when time and computer assets are limited. By taking advantage of the separability of the problem, we have shown how the computational complexity can be significantly reduced. Moreover, we have constructed a memory-efficient implementation and demonstrated it using synthetic data.

The method is robust against noise contamination and displays good super-resolution capabilities. The number of scattering centers to be localized is a user defined input (along with

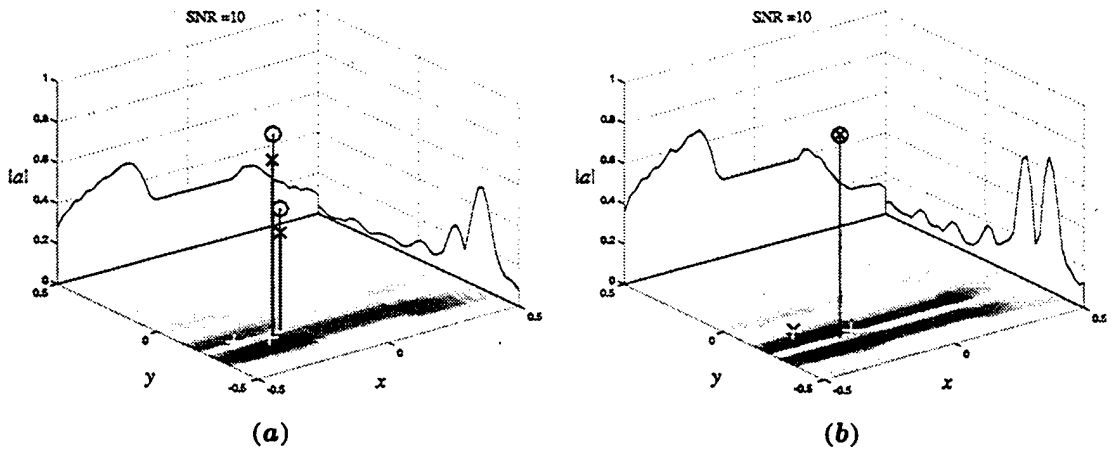

FIGURE 3. Super-Resolved Scattering Centers. In Figure 3(a) the point scatterers are separated by approximately $0.14\Delta x$ and $0.25\Delta y$ (where the resolution cell is $\Delta x \times \Delta y$ in size). Figure 3(b) shows the results of inappropriately associating two scatterers to a location where only one true scatterer actually exists.

seed estimates based on low resolution ISAR images) and the "best fit" location and strength of the scatterers are estimated according to Equations 15 and 21. Consequently, the approach appears to be well-suited to radar-based target identification problems that rely on template matching schemes in which only the information associated with the $\tilde{N}$ strongest scatterers are used.

Throughout, we have concentrated on the point scatterer model, but the method can be easily modified to include more complex cases (References 6 through 8). In many practical situations, however, data limitations and noise contamination issues can be expected to make such modifications ineffectual.

REFERENCES

1. A. W. Rihaczek and S. J. Hershkowitz. *Radar Resolution and Complex-Image Analysis.* Dedham Mass., Artech, 1996.
2. B. Borden. *Radar Imaging of Airborne Targets: A Primer for Applied Mathematicians and Physicists.* Philadelphia, IoP, 1999.
3. R. J. Sullivan. *Microwave Radar Imaging and Advanced Concepts.* Boston, Artech, 2000.
4. S. Hudson and D. Psaltis. "Correlation Filters for Aircraft Identification from Radar Range Profiles," *IEEE Trans. on Aerospace and Elect. Sys.,* Vol. 29 (1993), p. 741.
5. C. R. Smith and P. M. Goggans. "Radar Target Identification," *IEEE Antennas and Prop. Magazine,* Vol. 35, No. 2 (April, 1993), p. 27.
6. A. W. Rihaczek and S. J. Hershkowitz. "Man-Made Target Backscattering Behavior: Applicability of Conventional Radar Resolution Theory," *IEEE Trans. Aero. and Elect. Sys.,* Vol. 32, No. 2 (1996), p. 809.
7. M. J. Gerry, L. C. Potter, I. J. Gupta, and A. van der Merwe. "A Parametric Model for Synthetic Aperture Radar Measurements," *IEEE Trans. Antennas and Prop.,* Vol. 47, No. 7 (1999), p. 1179.
8. L. C. Potter and R. L. Moses. "Attributed Scattering Centers for SAR ATR," *IEEE Trans. Image Proc.,* Vol. 6, No. 1 (1997), p. 79.
9. P. M. Woodward. *Probability and Information Theory with Applications to Radar.* New York, Pergamon, 1953.
10. C. E. Cook and M. Bernfeld. *Radar Signals.* New York, Academic, 1967.
11. A. W. Rihaczek. *Principles of High-Resolution Radar.* New York, McGraw-Hill, 1969.
12. G. H. Golub and V. Pereyra. "The differentiation of pseudo-inverses and nonlinear least squares problems whose variables separate," *SIAM J. Numer. Anal.,* Vol. 10, No. 2 (1973), p. 413.
13. G. H. Golub and C. F. Van Loan. *Matrix Computations.* Baltimore, Johns Hopkins University Press, 1996.
14. C. T. Kelley. *Iterative Methods for Linear and Nonlinear Equations.* Philadelphia, SIAM, 1995.

Appendix

COMPUTER CODE FOR CALCULATING r AND ∇r

The following computer code was implemented in MATLAB and evaluates Equations 16, 24, and 25 for χ defined by Equation 9. The algorithm is:

1. Find $\chi = QR$ and set $\psi = Q^{\dagger}\eta$, $r = \|\psi(N+1:M)\|^2$.
2. Calculate $x = [R^{-1} \mid 0]\psi$ and $\zeta = Q \begin{bmatrix} 0 & 0 \\ 0 & I_{M-N} \end{bmatrix} \psi$.
3. $\Psi = \zeta^{\dagger} \nabla\chi$
4. $\nabla r = -2\mathrm{Re}(\Psi x)$.

function $[r, \nabla r] = r\_dr(z)$
global η N M T θ $\Delta\omega$ ω_0 a

| $\theta = [\theta_1, \theta_2, \ldots]^T$ vector of angles
| T = number of time measurements at each θ_j
| N = number of scattering centers
| M = number of observations (= T × length(θ))
| $z = [x_1, x_2, ..., x_N, y_1, y_2, ..., y_N]^T$
|
| $\nabla\chi$ = $M \times 2N$ array of derivatives
| Note, only the nonzero components are stored.

$\chi = \mathrm{zeros}(M, N)$; $\nabla\chi = \mathrm{zeros}(M, 2N)$;
$v = \mathrm{zeros}(M, 1)$; $\beta = \mathrm{zeros}(N, 1)$; $x = \mathrm{zeros}(N, 1)$; $\nabla r = \mathrm{zeros}(2N, 1)$;

| Obtain the orthogonal factorization of χ as $Q^{\dagger}\chi = R$ and $\psi = Q^{\dagger}\eta$.

$[\chi, \nabla\chi] = chi\_Dchi(z, \chi, \nabla\chi)$; $\psi = \eta$;
for $i = 1 : N$
  $[v(i:M), \beta(i)] = house(\chi(i:M, i))$;
  $\chi(i:M, i:N) = row\_house(\chi(i:M, i:N), v(i:M), \beta(i))$;
  $\psi(i:M) = row\_house(\psi(i:M), v(i:M), \beta(i))$;

| Save the Householder vectors in the lower triangle of χ (for later use)

  $\chi(i+1:M, i) = v(i+1:M)$;
end

| Calculate the residual.

$r = \|\psi(N+1:M)\|^2$;

| Computation of a (by Backsubstitution):
| $a = [R(1:N, 1:N)^{-1}\,\psi(1:N); \mathrm{zeros}(M-N, 1)]$;
| ($a(1:N)$ is also the scatterer strengths.)

$a(N) = \psi(N)/\chi(N, N)$;
for $i = N-1 : -1 : 1$
  $a(i) = (\psi(i) - \chi(i, i+1:N)\,a(i+1:N))/\chi(i, i)$;
end

| $\zeta = (I - P)\eta = Q\,[\mathrm{zeros}(N, 1); \psi(N+1:M)]$.
|
| Note, Q is stored in factored form: $Q = Q_1 \times Q_2 \times Q_3 \ldots Q_N$,

| so $Q^\dagger = Q_N^\dagger \ldots Q_3^\dagger \times Q_2^\dagger \times Q_1^\dagger$.

$\zeta = [\text{zeros}(N,1); \psi(N+1:M)]$;
for $i = N:-1:1$
  $v(i) = 1$; $v(i+1:M) = \chi(i+1:M, i)$;
  $\zeta(i:M) = row\_house(\zeta(i:M), v(i:M), \text{conj}(\beta(i)))$;
end

| $\Psi = \zeta^\dagger \nabla\chi$

$\Psi = \text{zeros}(2N, N)$;
for $i = 1:N$
  $\Psi(i,i) = \zeta^\dagger \nabla\chi(:,i)$; $\Psi(i+N,i) = \zeta^\dagger \nabla\chi(:,i+N)$;
end

| Finally, put it all together to calculate the gradient.

$\nabla r = -2\text{real}(\Psi a)$;

function $[v, \beta] = house(x)$

| Compute the Householder vector.
| (cf. §5.2.10 of Golub and Van Loan, third ed.)

$s = \|x\|\,(\text{sign}(x(1)) + (x(1) == 0))$; | require sign(0) = 1.
$v = x$;
if $s == 0$, $\beta = 1$; return, end
$v(1) = v(1) + s$;
$\beta = 1/(s^\dagger v(1))$;

function $A = row\_house(A, v, \beta)$

| Overwrites A with $Q_v A$ where $Q_v = I - \beta v v^\dagger$.

$w = A^\dagger v$;
$A = A - \beta\, v\, w^\dagger$;

function $[\chi, \nabla\chi] = chi\_Dchi(z, \chi, \nabla\chi)$
global η N M T θ $\Delta\omega$ ω_0

| Calculate χ and $\nabla\chi$.

$ct = \cos(\theta)$; $st = \sin(\theta)$;
$U = -z(1:N)\, st^T + z(N+1:2N)\, ct^T$; $V = z(1:N)\, ct^T + z(N+1:2N)\, st^T$;

for $k = 1:N$
  for $j = 1:M$
    $j_\theta = \text{ceil}(j/T)$;
    $t = (1 + \text{mod}(j-1, T))/T - .5 - U(k, j_\theta)$;
    $\nu = -V(k, j_\theta)$;
    $[\chi, D\chi] = amb\_Damb(t, \nu)$;

    $e = \exp(-\text{i}\nu\, t/2)$; | note: $\nu + 2v = v\ (= -\nu)$
    $\chi(j,k) = \chi\, e$;

    $a = -D\chi(1) + \text{i}\nu\, \chi/2$;
    $b = -D\chi(2) + \text{i}t\, \chi/2$;
    $\nabla\chi(j,k) = (-a\, st(j_\theta) + b\, ct(j_\theta))e$;
    $\nabla\chi(j, N+k) = -(a\, ct(j_\theta) + b\, st(j_\theta))e$;
  end
end

function $[\chi, D\chi] = amb\_Damb(t, \nu)$
global η N M T θ $\Delta\omega$ ω_0

| Calculate χ, $\partial\chi/\partial t$ and $\partial\chi/\partial\nu$

$\delta = \Delta\omega - |\nu|$; $sgn_\nu = \text{sign}(\nu) + (\nu == 0)$;

if $\delta < 0$, $\chi = 0$; $D\chi = 0$; return, end

$arg = \delta\, t/2$; $e = \exp(\mathrm{i}(\omega_0 + \nu/2)t)$;
$C = e\,\delta/\Delta\omega$; $sinc = \mathrm{sinc}(arg)$;

| Determine the ambiguity function

$\chi = C\, sinc$;

| Determine the derivatives

if $|arg| > 0$
  $sinc' = (\cos(arg) - sinc)/arg$;
else
  $sinc' = 0$;
end

if $\delta > 0$
  $D\chi(1) = \mathrm{i}(\omega_0 + \nu/2)\chi + C\,\delta\, sinc'/2$;
  $D\chi(2) = (\mathrm{i}t/2 - sgn_\nu/\delta)\chi - C\, sgn_\nu\, t\, sinc'/2$;
else
  $D\chi(1) = 0$;
  $D\chi(2) = -e\, sgn_\nu/\Delta\omega$;
end

INITIAL DISTRIBUTION

1 Office of Naval Research, Arlington
  ONR-313, W. Miceli
1 Naval War College, Newport (1E22, President)
1 Headquarters, 497 INOT, Falls Church (IOG Representative)
2 Defense Technical Information Center, Fort Belvoir
2 Center for Naval Analyses, Alexandria, VA (Technical Library)

ON-SITE DISTRIBUTION

4 Code 4TL000D (3 plus Archives copy)
8 Code 4T4100D
  B. Borden (5)
  S. Chesnut (1)
  G. Hewer (1)
  T. Loftus (1)
1 Code 452310D, W. Katzenstein
2 Code 452320D
  D. Reade (1)
  D. Roth (1)